Sensors and Materials, Vol. 34, No. 4 (2022) 1539–1547
MYU Tokyo

LETTER

S & M 2908

Detection and Localization of Small Defects in Large Glass-ceramics by Hybrid Macro and Micro Vision

Weixian Li,[1*] Zhen Wang,[1] Jie Deng,[2] and Sijin Wu[1]

[1]Beijing Information Science and Technology University,
No. 12 Qinghexiaoying East Road, Haidian District, Beijing, 100192, China
[2]Beijing Sevenstar Flow Co., Ltd.,
No. 8 Wenchang Avenue, Economic and Technological Development Zone, Beijing, 100176, China

(Received January 6, 2022; accepted February 22, 2022)

Keywords: defect detection, 3D localization, glass-ceramic, optical imaging

A method of hybrid macro and micro vision to detect and locate sub-millimeter defects in meter-sized glass-ceramics is proposed. A 3D localization model of defects with dual camera imaging and triaxial linear motion is established mathematically. The system is calibrated using a coarse-fine chessboard. A macroscopic camera with a large field of view is used to detect the 2D planar coordinates of possible defects in a large glass-ceramic, then a microscope with a small field of view is utilized to obtain the depth coordinates of these defects by image sharpness evaluation using the triaxial linear stage. Experiments show that the calibrated defect detection and localization system with hybrid macro and micro vision can detect and locate sub-millimeter defects in large glass-ceramics.

1. Introduction

Glass-ceramics have extraordinary thermal, electrical, optical, and mechanical properties. In particular, they have optical transparency and an ultralow (and sometimes even zero) expansion rate, resulting in their widespread application in astronomy and aerospace. However, in the manufacturing of glass-ceramics, defects, mainly bubbles produced by the melting process, inevitably arise. These defects degrade not only optical transparency but also fracture strength. Many studies have attempted to reveal the bubble generation mechanism and achieve bubble-free glass-ceramic production,[1–3] but defects in glass-ceramics remain widespread in the conventional manufacturing process. To realize defect-free glass-ceramics, it is necessary for defect detection and localization to be performed on-site. If the positions of defects are known, product quality can be objectively evaluated and the subsequent machining can be optimized. For example, if bubbles are located in a small corner of a glass-ceramic, a defect-free product can be obtained by removing this area. Therefore, it would be highly advantageous to find the defects of raw glass-ceramic materials and obtain their distributions in three dimensions.

Mass spectrometry, which identifies the constituents of a material by measuring the mass-to-charge ratio of ions, has been applied in glass bubble content inspection.[4] Raman spectroscopy using Raman spectra has also been employed.[5] Although the defect content may help elucidate

*Corresponding author: e-mail: liwx@bistu.edu.cn
https://doi.org/10.18494/SAM3792

ISSN 0914-4935

the bubble generation mechanism, the defect distribution is more useful in manufacturing. Ultrasonic tomography, X-ray tomography, and thermography are the most widely used defect inspection methods for composite materials.[6–11] However, owing to the contact of the ultrasonic couple with the substance under measurement, radiation damage by X-rays, and the low temperature sensitivity of glass-ceramics, these three methods are impracticable for inspecting defects in glass-ceramics in the workshop. Since glass-ceramics have excellent transparency, the reflection, refraction, or transmission of light is changed by defects, making an optical imaging method effective for glass-ceramic defect inspection.[12–17] Furthermore, only a camera is required for optical imaging, enabling the use of a very simple nondestructive and noncontact inspection system and making optical imaging the most common method for defect detection in glasslike materials.

In glass-ceramic manufacturing, although the raw product arriving from the furnace is usually very large with a diameter of about 1 m, the diameter of defects such as bubbles may be as small as 0.1 mm. The detection resolution of optical imaging with a single camera is insufficient to detect very small defects in a relatively large object. On the other hand, depth detection is difficult using a regular camera in visual inspection. In this article, a method of sub-millimeter defect detection and localization in meter-sized glass-ceramics using a hybrid of macro and micro vision is proposed. This method obtains the defect distribution in three dimensions, which can be applied in quality control and subsequent manufacturing.

2. Materials and Methods

2.1 3D localization

It is easy to observe where a defect lies in one plane and how big the defect is by optical imaging in either a large or small glass-ceramic. However, it is much more difficult to find the depth of a defect in a glass-ceramic. Owing to the small depth of field of a microscope, the defect depth can be detected by image sharpness evaluation in the procedure of microscopic depth scanning. A defect is localized when the sharpest image of the defect is found, and the distance from the defect to the upper surface of the glass-ceramic is defined as the defect depth. Although the microscope appears to be a suitable tool for the 3D localization of defects, it has a very small field of view of at most several millimeters, making it too slow for defect inspection over a piece of meter-sized glass-ceramic. Therefore, considering efficiency and functionality, a method for the detection and localization of small defects using a hybrid macro and micro vision is proposed for large glass-ceramics. A macroscopic camera with a large field of view at low magnification is used to capture macroscopic glass-ceramic images, with which the 2D planar coordinates of possible defects are calculated. A microscope with a small field of view at high magnification is used to compute the depth coordinate of the defects during depth scanning. Meanwhile, a triaxial linear stage moves in three dimensions and helps the microscope to find the top of the defects.

Figure 1 shows the coordinate systems of macro and micro vision for defect localization in a large glass-ceramic. A macroscopic camera is fixed to observe the whole glass-ceramic, and a microscope, which is mounted on a triaxial linear stage and is moveable in three dimensions, is

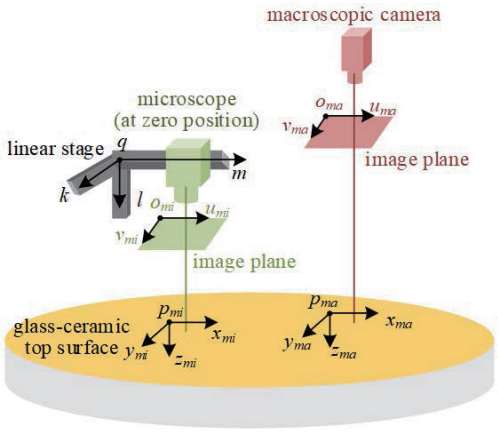

Fig. 1. (Color online) Coordinate systems of macro and micro vision.

at the depth where it can capture the sharpest image of the glass-ceramic's surface (defined as the zero position). o_{mi}-$u_{mi}v_{mi}$ and o_{ma}-$u_{ma}v_{ma}$ are the micro and macro image coordinate systems, with the origin at the top left of their images, respectively. The top-left point p_{mi} of the object field of view of the microscope at the zero position is set as the origin and p_{mi}-$x_{mi}y_{mi}z_{mi}$ is the micro object coordinate system, with $p_{mi}x_{mi}$ parallel to $o_{mi}u_{mi}$, $p_{mi}y_{mi}$ parallel to $o_{mi}v_{mi}$, and $p_{mi}z_{mi}$ as the depth direction. On the same plane of p_{mi}-$x_{mi}y_{mi}$, the top-left point p_{ma} of the object field of view of the macroscopic camera is set as the origin and p_{ma}-$x_{ma}y_{ma}z_{ma}$ is defined as the macro object coordinate system. Similarly, $p_{ma}x_{ma}$ is parallel to $o_{ma}u_{ma}$, $p_{ma}y_{ma}$ is parallel to $o_{ma}v_{ma}$, and $p_{ma}z_{ma}$ is the depth direction. First, the imaging of microscope and macroscopic camera is simplified using the following equation:

$$\begin{bmatrix} x_t \\ y_t \end{bmatrix} = \beta_t \begin{bmatrix} u_t \\ v_t \end{bmatrix}, t = \{mi, ma\}, \tag{1}$$

where β_{mi} and β_{ma} are the magnifications of the microscope and macroscopic camera, respectively, in the unit of mm/pixel.

The position relationship between the micro object coordinate system at zero position and the macro object coordinate system is described as

$$\begin{bmatrix} x_{mi} \\ y_{mi} \end{bmatrix} = \begin{bmatrix} \cos\theta & \sin\theta \\ -\sin\theta & \cos\theta \end{bmatrix} \begin{bmatrix} x_{ma} \\ y_{ma} \end{bmatrix} + \begin{bmatrix} \Delta x \\ \Delta y \end{bmatrix}, \tag{2}$$

where θ is the rotation angle and Δx and Δy are the offsets in the x and y directions, respectively. In this paper, we suppose that all the depth directions (Z axis) are parallel after system leveling; thus, $z_{mi} = z_{ma}$.

Driven by the triaxial linear stage, the microscope moves within the field of view of the macroscopic camera and its 3D moving coordinate system is q-mkl, as shown in Fig. 1. We suppose that ql is strictly parallel to $p_{mi}z_{mi}$, resulting in the expression

$$\begin{bmatrix} \Delta x_{mi} \\ \Delta y_{mi} \end{bmatrix} = \begin{bmatrix} \cos\varphi & \sin\varphi \\ -\sin\varphi & \cos\varphi \end{bmatrix} \begin{bmatrix} \Delta m \\ \Delta k \end{bmatrix}, \tag{3}$$

where φ is the rotation angle, Δx_{mi} and Δy_{mi} are the movement distances of the microscope in the $p_{mi}x_{mi}$ and $p_{mi}y_{mi}$ directions, and Δm and Δk are the stepping values of the linear stage in the X and Y directions, respectively.

The macroscopic camera first finds the location of a defect on the glass-ceramic surface, (x_{ma}, y_{ma}), and guides the microscope moving along XY directions of the linear stage to arrive on the top of the defect. Then, the microscope scans the glass-ceramic in the Z direction and outputs the depth of the defect. If the linear stage moves a distance of Δl along the Z direction from the zero position to obtain the sharpest defect image, then the defect depth is

$$z_{ma} = n\Delta l\,, \tag{4}$$

where n is the refractive index of the glass-ceramic. Thus, the defect is located at (x_{ma}, y_{ma}, z_{ma}) by the dual camera imaging and triaxial linear motion.

2.2 System calibration

For the proposed 3D localization, the parameters in Eqs. (1)–(3) must be calibrated. A coarse-fine chessboard target with coarse and fine grids of an accurately known size and relative position, as shown in Fig. 2, is designed. The calibration of the system has three main steps.

Firstly, β_{mi} and β_{ma} in Eq. (1) are calculated on the basis of the images of the target with fine and coarse grids, both with a known size. Secondly, θ, Δx, and Δy in Eq. (2) are calculated on the basis of the images of the target with the known relative position of the coarse and fine grids. An intermediate coordinate system with the origin at the top-left corner of the coarse-fine chessboard is set as p_w-$x_w y_w$ with $p_w x_w$ parallel to the chessboard rows and $p_w y_w$ parallel to the chessboard columns. Their relationships with the micro and macro object coordinate systems are expressed by

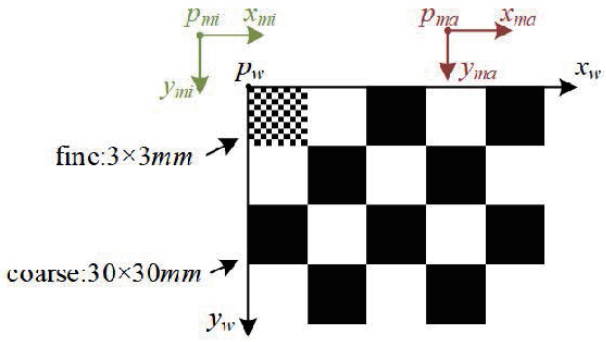

Fig. 2. (Color online) Coarse-fine chessboard target.

$$\begin{bmatrix} x_{mi} \\ y_{mi} \end{bmatrix} = \begin{bmatrix} \cos\theta_1 & \sin\theta_1 \\ -\sin\theta_1 & \cos\theta_1 \end{bmatrix} \begin{bmatrix} x_w \\ y_w \end{bmatrix} + \begin{bmatrix} \Delta x_1 \\ \Delta y_1 \end{bmatrix}, \tag{5}$$

and

$$\begin{bmatrix} x_{ma} \\ y_{ma} \end{bmatrix} = \begin{bmatrix} \cos\theta_2 & \sin\theta_2 \\ -\sin\theta_2 & \cos\theta_2 \end{bmatrix} \begin{bmatrix} x_w \\ y_w \end{bmatrix} + \begin{bmatrix} \Delta x_2 \\ \Delta y_2 \end{bmatrix}, \tag{6}$$

where θ_1 and θ_2 are the rotation angles, and $\Delta x_1/\Delta y_1$ and $\Delta x_2/\Delta y_2$ are the offsets in the x/y directions. With at least two corresponding corners of the fine and coarse grids, the parameters in Eqs. (5) and (6) can be easily solved. Then, we obtain

$$\begin{cases} \theta = \theta_1 - \theta_2, \\ \Delta x = \Delta x_1 - \cos(\theta_1 - \theta_2)\Delta x_2 - \sin(\theta_1 - \theta_2)\Delta y_2, \\ \Delta y = \Delta y_1 + \sin(\theta_1 - \theta_2)\Delta x_2 - \cos(\theta_1 - \theta_2)\Delta y_2. \end{cases} \tag{7}$$

Finally, φ in Eq. (3) is calculated by observing the grid corners moving on the microscopic image when the linear stage moves a certain distance along the X or Y direction.

3. Experiments and Results

A defect detection and localization setup using a hybrid macro and micro vision for a glass-ceramic is developed, as shown in Fig. 3(a). A macroscopic camera with a focal length of 25 mm and image resolution of 5472 × 3648 pixels is used to calculate the planar coordinates of possible

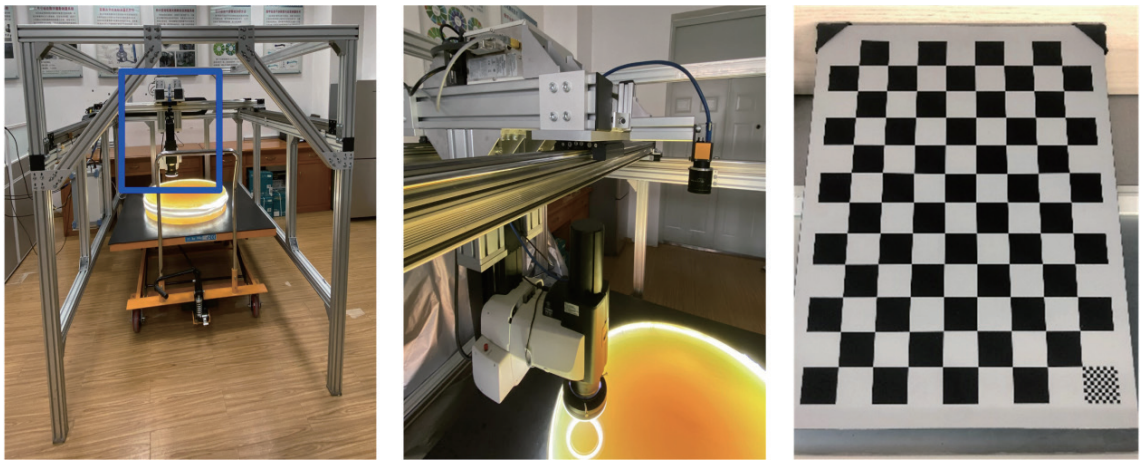

(a) (b) (c)

Fig. 3. (Color online) Experimental system: (a) experimental setup, (b) dual cameras, and (c) chessboard target.

defects, and a Nikon SMZ25 stereo microscope equipped with a camera (2592 × 1944 pixels) on its left stereo light path is utilized to perform depth localization. The setup is illustrated in Figs. 3(a) (marked by blue rectangle) and 3(b). To detect and locate sub-millimeter defects in meter-sized glass-ceramics, the field of view of the macroscopic camera is set to about 0.25 × 0.18 m^2, and the hybrid module of the macroscopic camera and microscope is installed on an *XY* linear stage to detect defects in 1 m by scanning. Because the SMZ25 microscope has a motorized focus unit, the microscope is moveable in three directions. Differently from in Sect. 2.1, the macroscopic camera is not fixed in the setup and can move in the *X* and *Y* directions to increase the detection area. In the macroscopic camera's every detection spot, the dual camera localization module is the same as that in Sect. 2.1 and can obtain the 3D positions of defects in the entire macro object coordinate system. Wtih the known moving distance of the macroscopic camera, the found defect positions can be transformed to the first macroscopic camera spot and be shown together. The range of 3D motion of the macroscopic camera is 1 × 1 × 100 mm^3.

After the coarse-fine chessboard target, shown in Fig. 3(c), is placed at a location where the microscope can observe the fine grid and the macroscopic camera can observe the coarse grid, two images are simultaneously taken by the dual cameras, and the two magnifications for the setup illustrated in Fig. 3 are calculated as β_{mi} = 0.0089 mm/pixel and β_{ma} = 0.0550 mm/pixel. In accordance with the procedure described in Sect. 2.2, rotation angle θ = 0.0169 rad, offset Δx = −109.55 mm, offset Δy = 121.03 mm, and rotation angle φ = −0.0003 rad are calibrated.

A glass-ceramic cylinder of 0.7 m diameter is inspected to locate defects within 15 mm from the surface, corresponding to the reflective coating of an astronomical mirror. The side of the glass-ceramic is unpolished, but its top surface is well polished, allowing light to propagate inside. A long flexible white LED ring light with power of 30 W/m is adhered to the side to provide sufficient illumination. Figure 4(a) is the macro vision image taken at the first spot by the macroscopic camera and Fig. 4(b) shows eight bubbles extracted by Canny edge extraction and a round geometric constraint. The No. 3 bubble in the blue rectangle, which is enlarged in Fig. 4(c), is taken as an example. Its planar coordinates in the macro object coordinate system are obtained as (34.07, 134.75 mm) using Eq. (1), which are transformed to (−73.20, 255.19 mm) in the micro object coordinate system using Eq. (2). According to Eq. (3), the linear stage should move −84.71 mm along its *X* stage direction and 246.53 mm along its *Y* stage direction so that the No. 3 bubble is at the center of the microscopic field of view. The microscopic image captured

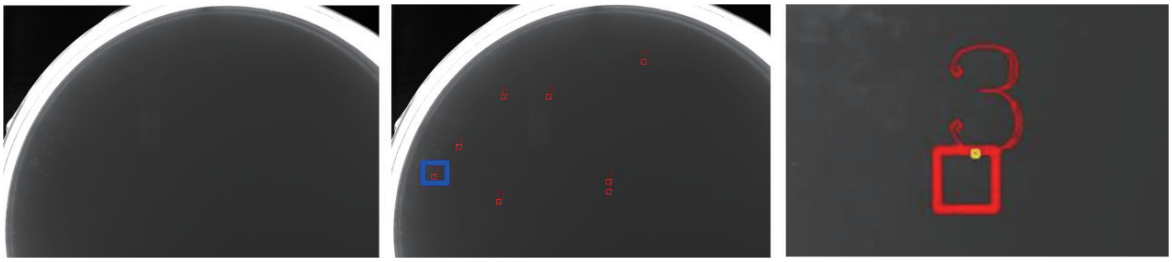

(a) (b) (c)

Fig. 4. (Color online) Macro vision images: (a) raw image, (b) eight defects, and (c) No. 3 defect.

after the microscope reaches the top of the No. 3 bubble is shown in Fig. 5(a), with the bubble located inside the blue rectangle. An enlargement of the bubble is shown in Fig. 5(b). For better visualization, part of the microscopic scanning image sequence is illustrated in Fig. 6. The first row shows five raw images taken at five depths, and the second row shows their sharpness evaluation results. Since the SMZ25 is a Greenough-type stereo microscope, the bubble is moving in the microscopic image and the red rectangle is obtained by a large change in the grayscale of the images between two subsequent depths. The sharpness is only evaluated in the moving red rectangle, with the sharpness value SV defined as

$$SV = mean[\nabla^2(I)], \tag{8}$$

where I is the image in the red rectangle, $mean(\bullet)$ is the average operator, and $\nabla^2(\bullet)$ is the Laplace operator. Table 1 shows the sharpness value, stage movement (visual depth) Δl, and real depth z_{ma} of these five images with a refractive index of 1.54. The image shown in Fig. 6(c) is the sharpest. Therefore, the No. 3 bubble is located at (34.07, 134.75, 9.73 mm). All the other bubbles can be located after the microscope is moved by the XYZ linear stage, and the 3D defect

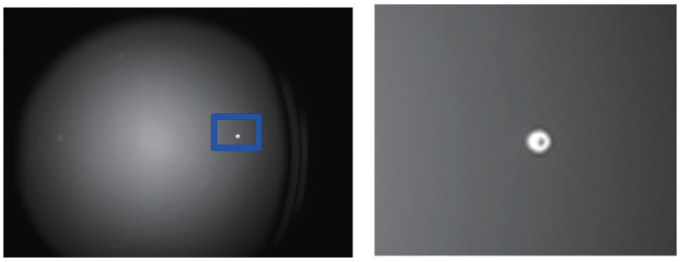

(a) (b)

Fig. 5. (Color online) Micro vision images: (a) raw image and (b) No. 3 defect.

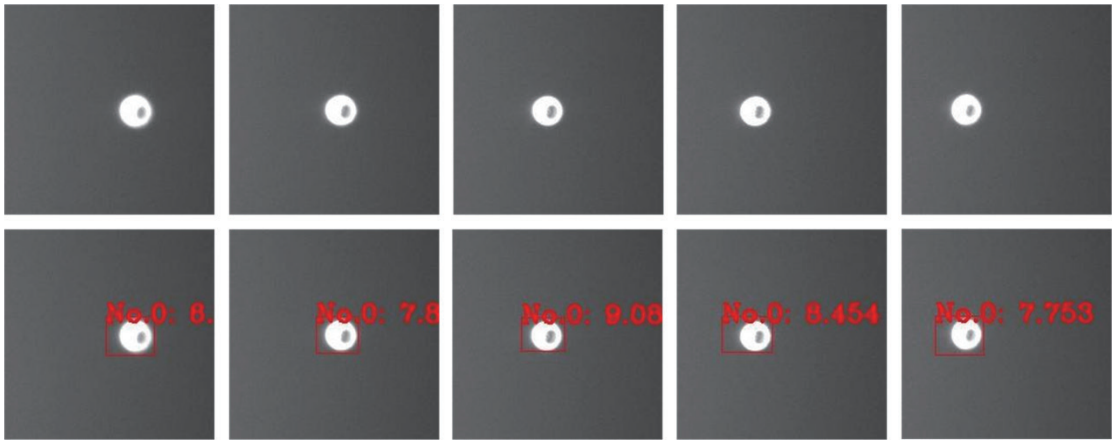

(a) (b) (c) (d) (e)

Fig. 6. (Color online) Micro vision image sequence: (a) @7.78, (b) @8.76, (c) @9.73, (d) @10.70, and (e) @11.67 mm.

Table 1
Results of five images at five depths.

Image	SV	Δl	z_{ma}
(a)	6.358	5.05	7.78
(b)	7.885	5.69	8.76
(c)	9.083	6.32	9.73
(d)	8.454	6.95	10.70
(e)	7.753	7.58	11.67

Table 2
3D locations of eight bubbles in Fig. 4(b).

Bubble	Location (mm)	Bubble	Location (mm)
0	(85.05, 156.94, 5.84)	4	over 15 mm from the surface
1	over 15 mm from the surface	5	over 15 mm from the surface
2	over 15 mm from the surface	6	(90.11, 73.43, 12.16)
3	(34.07, 134.75, 9.73)	7	(198.44, 46.29, 4.86)

distribution of this glass-ceramic can be obtained in the macro object coordinate system. Table 2 shows the 3D locations of the eight bubbles in Fig. 4(b). Since only defects within 15 mm from the surface are scanned and detected, the Nos. 0, 3, 6, and 7 bubbles are all located. These four bubbles are defects in the reflective coating.

4. Conclusions

A method for the detection and localization of small defects in a large glass-ceramic using hybrid macro and micro vision is proposed. The 3D localization system with dual cameras and a triaxial linear stage is modeled mathematically and calibrated using a coarse-fine chessboard target, and a prototype is developed. The 3D positions of defects can be obtained, and the system can be employed by engineers during the manufacture of glass-ceramics. Since the positions of detected defects are described in the macro object coordinate system, future work will be carried out to transform them to the coordinate system of the glass-ceramic.

Acknowledgments

This work is supported by the National Natural Science Foundation of China (Grant Nos. 52075044 and 52075045) and Key Cultivation Projects of Beijing Information Science and Technology University (2121YJPY206).

References

1 O. Peitl, E. D. Zanotto, and K. Heide: Ceram. Int. **46** (2020) 22513. https://doi.org/10.1016/j.ceramint.2020.06.011
2 D. Bolore and F. Pigeonneau: J. Am. Ceram. Soc. **101** (2018) 1892. https://doi.org/10.1111/jace.15361
3 L. Pereira, O. Podda, B. Fayard, A. Laplace, and F. Pigeonneau: J. Am. Ceram. Soc. **103** (2020) 2453. https://doi.org/10.1111/jace.16950
4 C. Gago, R. Pereiro, N. Bordel, P. Ramos, A. Tempez, and A. Sanz-Medel: Anal. Chim. Acta **652** (2009) 272. https://doi.org/10.1016/j.aca.2009.06.038

5 S. Moraes, D. Morgado, and M. Nali: Vib. Spectrosc. **100** (2019) 57. https://doi.org/10.1016/j.vibspec.2018.10.010
6 G. P. M. Fierro and M. Meo: Ultrasonics **93** (2019) 43. https://doi.org/10.1016/j.ultras.2018.10.011
7 M. Bor, K. Tom*až*, and G. Janez: Stroj Vestn-J. Mech. Eng. **63** (2018) 147. https://doi.org/10.5545/sv-jme.2015.2988
8 V. Virginia, H. Ulrich, A. Richard, S. Michael, U. Norman, and B. Christoph J: Prog. Photovolt. **23** (2015) 124. https://doi.org/10.1002/pip.2411
9 W. H. Harris, D. P. Guillen, J. Klouzek, R. Pokorny, T. Yano, S. Lee, M. J. Schweiger, and P. Hrma: J. Am. Ceram. Soc. **100** (2017) 3883. https://doi.org/10.1111/jace.14895
10 M. Yumnam, H. Gupta, D. Ghosh, and J. Jaganathan: Constr. Build. Mater. **310** (2021) 125265. https://doi.org/10.1016/j.conbuildmat.2021.125265
11 H. Wang and S.-J. Hsieh: Proc. of SPIE: Thermosense: Thermal Infrared Applications XXXVII (SPIE 2015) 9485. https://doi.org/10.1117/12.2176537
12 Z. Chen, C. Zhao, Y. Shen, P. Li, X. Wang, and Z. Ding: Opt. Commun. **341** (2015) 122. https://doi.org/10.1016/j.optcom.2014.12.016
13 S. Zhang, J. Bai, K. Wang, F. He, and B. Zhou: Proc. SPIE: AOPC 2015: Optical Test, Measurement, and Equipment (SPIE 2015) 9677. https://doi.org/10.1117/12.2199047
14 D.-B. Perng, C.-C. Chou, and W.-Y. Chen: JCIIE **24** (2007) 341. https://doi.org/10.1109/ICMECH.2005.1529331
15 G. A. De Vitis, A. Di Tecco, P. Foglia, and C. A. Prete: J. Imaging **7** (2021) 223. https://doi.org/10.3390/jimaging7110223
16 M. Chang, Y. C. Chou, P. T. Lin, and J. L. Gabayno: Int. J. Disturb. Sens. Netw. **42** (2014) 125. https://doi.org/10.1155/2014/634748
17 D. Steiner and R. Katz: J. Comput. Inf. Sci. Eng. **7** (2007) 85. https://doi.org/10.1115/1.2424244